JGR Space Physics

RESEARCH ARTICLE
10.1029/2021JA029495

Discrete Aurora on Mars: Spectral Properties, Vertical Profiles, and Electron Energies

Lauriane Soret[1], Jean-Claude Gérard[1], Nicholas Schneider[2], Sonal Jain[2], Zachariah Milby[2], Birgit Ritter[1,3], Benoît Hubert[1], and Tristan Weber[4,5]

[1]Laboratoire de Physique Atmosphérique et Planétaire (LPAP), Université de Liège, Institut STAR, Liège, Belgium, [2]Laboratory for Atmospheric and Space Physics, University of Colorado Boulder, Boulder, CO, USA, [3]Observatoire Royal de Belgique, Bruxelles, Belgium, [4]Solar System Exploration Division, NASA GSFC, Greenbelt, MD, USA, [5]Department of Physics and Astronomy, Howard University, Washington, DC, USA

This article is a companion to Schneider et al. (2021), https://doi.org/10.1029/2021JA029428.

Key Points:

- N_2 Vegard-Kaplan bands have been detected in the ultraviolet Martian aurora
- The presence of crustal magnetic field does not influence the altitude of the auroral emission peak
- Green line intensities up to a few kilorayleighs are expected in regions of crustal magnetic field and may be visible with the naked eye

Correspondence to:
L. Soret,
lauriane.soret@uliege.be

Citation:
Soret, L., Gérard, J.-C., Schneider, N., Jain, S., Milby, Z., Ritter, B., et al. (2021). Discrete aurora on Mars: Spectral properties, vertical profiles, and electron energies. *Journal of Geophysical Research: Space Physics*, *126*, e2021JA029495. https://doi.org/10.1029/2021JA029495

Received 28 APR 2021
Accepted 5 AUG 2021

Abstract We present an analysis of hundreds of middle ultraviolet auroral spectra collected at the limb with the Imaging UltraViolet Spectrograph (IUVS) instrument on board the Mars Atmosphere and Volatile EvolutioN (MAVEN) spacecraft. While the companion paper by Schneider et al. (2021), https://doi.org/10.1029/2021JA029428 focuses on the detection, location, and occurrence frequency of discrete auroral events, this study addresses the spectral properties and vertical profiles of the auroral emissions. Our independent selection of events is based on a combination of automatic and manual detection methods with adequate signal-to-noise ratio of both the CO Cameron bands and the CO_2^+ ultraviolet doublet (UVD) at 190–270 and 288–289 nm, respectively. We find that the ratio of these two features remains quasi-constant for UVD intensities exceeding ~200 rayleighs (R), but the CO Cameron/CO_2^+ UVD ratio may become increasingly large for low UVD intensities. Three weak N_2 Vegard-Kaplan bands are identified in the Martian aurora for the first time. Limb profiles of the [OI] line at 297.2 nm indicate that the visible oxygen green line brightness may reach a few kilorayleighs. The distribution of the altitude of the emission peaks in the aurora is identical in and out of the region of crustal magnetic field located in the southern hemisphere. Comparisons of in situ measurements of electron energy spectra and ultraviolet auroral detections have been made for five optical detections. They generally show temporal coincidence but not necessarily quantitative agreement with the altitude and brightness expected from the characteristics of the measured electron energy spectra.

Plain Language Summary The MAVEN spacecraft has been orbiting Mars since September 2014 to study its upper atmosphere, ionosphere, and interaction with the solar wind. We focus on the discrete aurorae, previously discovered from the Mars Express orbiter. Discrete aurorae are observed on the nightside and are localized both in space and time. We analyze the ultraviolet spectra observed at the limb with the Imaging Ultraviolet Spectrograph to determine the main characteristics of these aurorae. We show that the emission peaks occur at ~130 km. They are composed of several emissions, such as CO, CO_2^+, N_2, and atomic oxygen. We find that they occur more often in the presence of strong crustal magnetic field. We also deduce that the altitude of the aurora is independent of many parameters except for seasons. We analyze the intensity ratio of these emissions and show that anomalies occur in the ratio of the CO Cameron bands to the CO_2^+ UV doublet at low intensity. Finally, we compare the detection of auroral events with the presence of strong electron precipitation measured on board MAVEN. A temporal correlation is generally observed but association of the electron flux and specific UV auroral detection is not always clear because measurements are not colocated.

1. Introduction

Since 2005, Mars has progressively revealed that its atmosphere is glowing with several types of aurorae. So far, three types of aurorae have been observed in the Martian atmosphere: discrete aurorae, diffuse aurorae, and proton aurorae.

Chronologically, discrete aurorae were first discovered with the Spectroscopy for the Investigation of the Characteristics of the Atmosphere of Mars (SPICAM) instrument on board European Space Agency's (ESA)

Mars Express spacecraft (Bertaux et al., 2005, 2006). They occur on the Martian nightside and are very localized both in time and space. Discrete aurorae will be further described and analyzed later in this work.

Diffuse aurorae were identified in 2015 with the IUVS instrument (Schneider et al., 2015) on board NASA's MAVEN spacecraft. Like the discrete aurorae, they are observed on the nightside of the planet. However, diffuse aurorae are widespread features which can cover Mars' entire nightside. One such global event was observed in September 2017 (Schneider et al., 2018). Diffuse aurorae are correlated with solar energetic particles.

Finally, proton aurorae were detected with IUVS (Deighan et al., 2018). Ritter et al. (2018) found additional events in the Mars Express SPICAM database and showed that solar events such as coronal mass ejections (CME) and/or corotating interaction regions (CIR) trigger proton aurorae. Contrary to discrete and diffuse aurorae, proton aurorae occur on the dayside. They are caused by the direct interaction of the solar wind protons with the Martian corona and further interaction of protons and energetic hydrogen atoms with the upper atmosphere. They are the most common type of aurora on Mars.

This study focuses on discrete aurorae. Bertaux et al. (2005) detected a strong discrete auroral emission peak lasting seven seconds during a limb observation of SPICAM on the nightside. Its spectral composition was quite different from the previously observed nitric oxide nightglow emission in the same wavelength range. This averaged discrete auroral spectrum was characterized by the presence of the CO ($a^3\Pi$-$X^1\Sigma$) Cameron bands between 190 and 270 nm, the CO ($A^1\Pi$-$X^1\Sigma^+$) fourth positive system (CO 4P) between 135 and 170 nm, the CO_2^+ ($B^2\Sigma_u^+$-$X^2\Pi_g$) doublet at 289 nm, the [OI] at 297.2 nm and the OI 130.4 nm triplet emissions. Bertaux et al. (2005) noticed that this aurora was located at the boundary between open and closed magnetic field lines of the crustal Martian magnetic field (located in the southern hemisphere between ~150° and 210° longitude) in a cusp-like region. They proposed that discrete aurorae could be produced by the interaction of energetic electrons moving along crustal magnetic field lines, exciting the CO_2 molecules that dominate the composition of Mars' upper atmosphere.

Leblanc et al. (2008) further searched for other auroral signatures in both limb and nadir SPICAM observations. They identified nine additional detections on the Mars nightside (one at the limb and eight in the nadir direction), in six Mars Express orbits spread over the database. They could quantify the brightness of CO Cameron bands emission and, in some cases, the CO_2^+ UVD. They compared the locations of the detections to a map displaying the probability of open field lines at 400 km altitude calculated by Brain et al. (2007) based on electron pitch angle distribution measurements by Mars Global Surveyor. They confirmed that discrete aurorae occur in the presence of cusp-like magnetic field line structures. After 10 years of operations of the SPICAM instrument, Gérard et al. (2015) reexamined the nadir observations while Soret et al. (2015) focused on the limb data. They compiled a list of 19 discrete aurorae (16 observed in the nadir mode and 3 at the limb). These observations also confirmed that the Mars discrete aurorae observed with SPICAM are located in magnetic cusp-like structures in the southern hemisphere. They evaluated several parameters of the discrete aurorae. They deduced that a discrete aurora could last at least the time duration of the limb observation, that is a few tens of seconds. They estimated the latitudinal size of the aurorae to be from 21 to 125 km wide, with a mean size value of 44 km. The CO ($a^3\Pi$-$X^1\Sigma$) Cameron bands, the CO ($A^1\Pi$-$X^1\Sigma^+$) fourth positive system, the CO_2^+ ($B^2\Sigma_u^+$-$X^2\Pi_g$) UVD, the OI multiplets at 297.2 nm and at 130.4 nm were detected in the limb spectra. Their mean intensities were 2525, 648, 494, 360, and 31 R, respectively, and presented a very large variability. The 135.6 nm OI emission could not be detected, though. The altitude of the CO Cameron bands auroral emission was found to be 137 ± 27 km.

The NASA Mars Atmosphere and Volatile EvolutioN (MAVEN) spacecraft has been orbiting Mars since September 21, 2014. The Imaging UltraViolet Spectrograph (IUVS; McClintock et al., 2015) instrument aims to study Mars' upper atmosphere in the far-UV (110–190 nm; FUV) and middle-UV (180–340 nm; MUV). The companion paper by Schneider et al., 2021; (hereafter Schneider21) analyzes the entire IUVS data set and identifies no fewer than 278 discrete aurorae. Schneider21 confirms that many of the discrete auroral events occur at the vicinity of a crustal magnetic field. More than 18% of the detections occur in the strong crustal magnetic field structures (between 150° and 210° longitude and −30° to 60° south latitude), where all the auroral SPICAM observations have been detected. However, thanks to the higher sensitivity of the IUVS instrument and increased spatial coverage, the authors unexpectedly also detect discrete aurorae

outside of the crustal magnetic field structure, in the northern hemisphere. They also show that discrete aurorae are brighter in the strong magnetic field area and tend to statistically occur more often in the evening than in the morning, when the *By* component of the Interplanetary Magnetic Field is negative.

In this study, we present new statistical results for the Martian discrete aurorae based on the MAVEN/IUVS data set that will be described in Section 2. In Section 3, we analyze limb spectra to retrieve intensities of the CO Cameron bands, the CO_2^+ UVD, the [OI] 297.2 nm line and the N_2 Vegard-Kaplan (VK) system. We also determine the altitude distribution of these auroral emissions. We examine correlations between the emissions and provide possible explanations of the observed variations. In particular, we focus on the CO Cameron/CO_2^+ UVD brightness ratio and compare it to the extensively observed dayglow emission. Finally, Section 4 presents electron energy spectra measured with the Solar Wind Electron Analyzer (SWEA) instrument (Mitchell et al., 2016) on board MAVEN in conjunction with IUVS measurements of discrete aurorae.

2. The MAVEN-IUVS Auroral Data Set

2.1. The IUVS Instrument

The MAVEN spacecraft moves along an elliptical orbit with a periapsis located at an altitude of ~150–200 km. The limb observations analyzed in this study have been acquired near periapsis with the IUVS spectral imager. During a single orbit, IUVS generally records up to 12 limb scans divided into 21 vertical mirror positions, each recording seven spectra along the slit (see also Schneider21 for additional description). The slit is usually slightly tilted relative to the horizon so the seven spatial bins give a combination of horizontal and vertical information. The instrument records emission spectra of the Martian atmosphere in the far-ultraviolet and mid-UV regions. This study focuses on the MUV part of the observations. IUVS spectra have been corrected for detector dark current and have been background subtracted and calibrated in physical units. The MUV brightness data carry an estimated systematic uncertainty of 30%. Level 1 C (L1C; Schneider et al., 2020; Schneider21) cleaned data, archived with the NASA Planetary Data System (PDS), have been used to detect auroral signatures (see Section 2.2) and quantify the auroral emissions (see Section 3).

2.2. Data Selection

A large amount of data have been collected by IUVS since the beginning of the mission in 2014. Some criteria were used to reduce the acquired spectra in all nightside observations to those with a significant probability of an auroral signature. For orbits up to number 10,000, only observations unambiguously acquired on the night side were considered: spectra collected at a solar zenith (SZA) value at the tangent point less than 105° were discarded to avoid any daytime contamination. In this study, all IUVS nightside spectra have been processed individually in order to derive limb brightness profiles, contrary to Schneider21 which sums up individual spectra from a given scan to obtain a composite spectrum with an increased signal-to-noise ratio (SNR). Subsequently, individual spectra have been compared to a reference discrete auroral spectrum. Only those with a linear Pearson correlation coefficient higher than 0.5 were retained for a "by-eye" confirmation that they correspond to an auroral feature (Gérard et al., 2015), as described hereafter (see Figure 1).

Figure 1b shows an example of an observed individual spectrum represented by a red line. This spectrum is compared to the discrete auroral reference spectrum in blue (from orbit 8687 at 18:27 UTC). It is also compared to a nitric oxide reference spectrum from Stiepen et al. (2017) since NO nightglow emission exhibits a somewhat similar spectral distribution and can also be present on the Martian nightside. The main difference can be observed at 215.8 nm where the strong (0, 1) CO Cameron band is shifted to slightly longer wavelengths compared to the (0, 3) NO delta band, and also at 221.9 nm where the NO (0, 4) band is present but no feature can be observed in the discrete auroral spectrum. The discrete auroral emission also usually includes the CO_2^+ UVD emission at 288–289 nm, while the NO emission does not exhibit a strong spectral signature beyond 275 nm.

Visual confirmation was also constrained by a bigger picture. We use the detector image from which the analyzed spectrum was extracted (Figure 1a) to check that an auroral event was indeed occurring at that time: a bright auroral signal has to be observed in several spatial bins of the detector image. Figure 1a confirms that the CO Cameron bands (on the left part of the image detector) and the CO_2^+ UVD (on the right

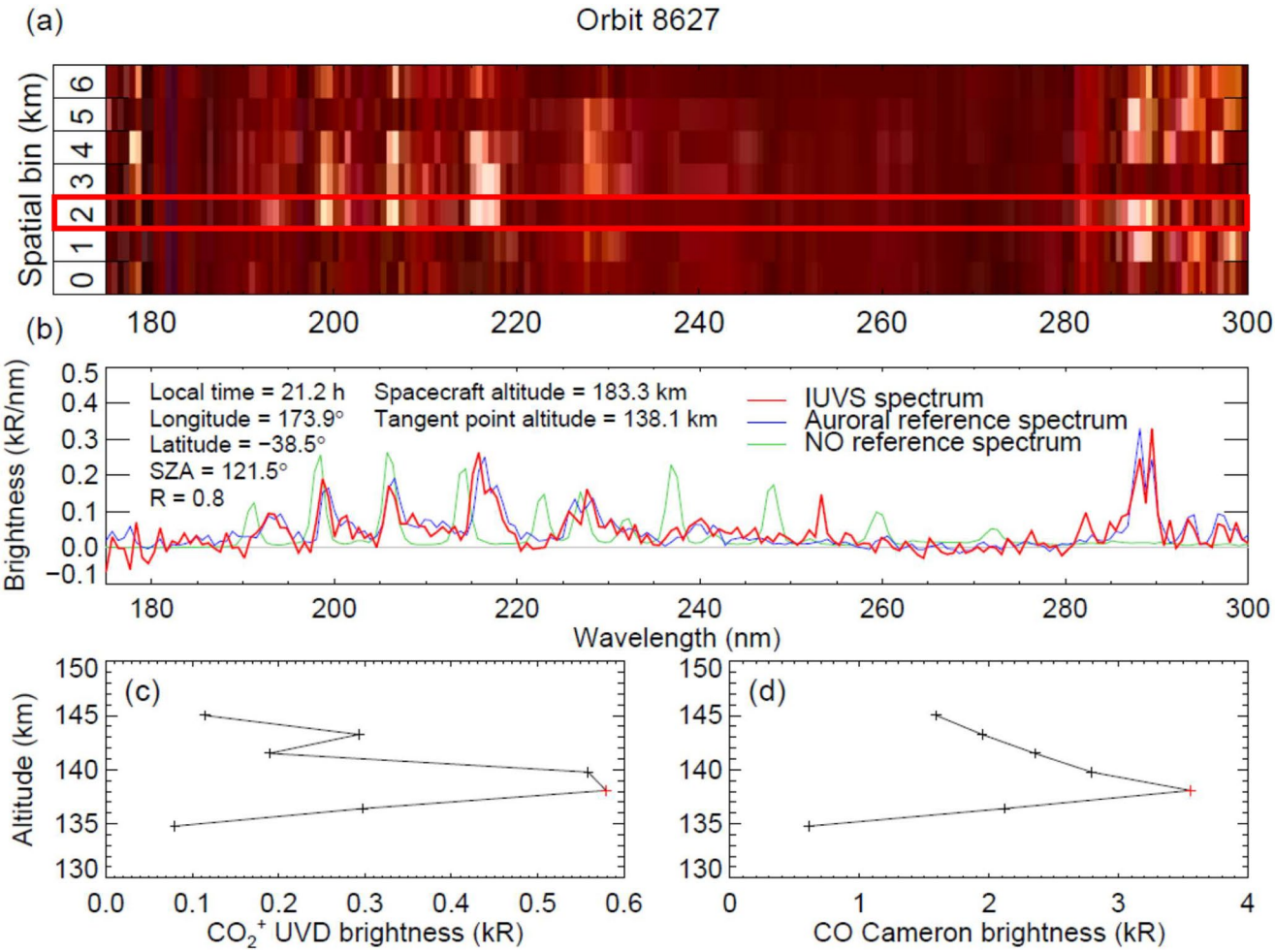

Figure 1. (a) Image of the Mars Atmosphere and Volatile EvolutioN/Imaging UltraViolet Spectrograph (MAVEN/IUVS) detector during an auroral event (orbit 8627, February 28, 2019, 13:11 UTC). The horizontal axis represents the wavelength while the vertical axis corresponds to the length of the spectrograph slit. (b) The spectrum plotted in red is extracted from the indicated spatial bin along the slit of the image detector (red rectangle). As a comparison, a reference discrete auroral spectrum is plotted in blue and a NO nightglow reference spectrum is shown in green. (c) Limb profile of the CO_2^+ UVD emission extracted from the image detector. The red plus symbols correspond to the values retrieved from the observed spectrum (red rectangle in panel (a) and red spectrum in panel (b)). (d) Same for the CO Cameron emission.

part) are present from top to bottom. Figure 1 thus shows a confirmed discrete auroral spectrum obtained during orbit 8627 on February 28, 2019 at 13:11 UTC.

A total of 1,452 spectra, spread over 192 limb scans and 66 orbits have passed this by-eye confirmation test. These detections are represented by white circles in Figure 2a, where they are overlaid on top of the statistical map of probability of observing open/closed magnetic field lines (Brain et al., 2007). This color-coded map was derived from the magnetometer/electron reflectometer measurements on board the Mars Global Surveyor MGS, and is based on electron pitch angle distributions at about 400 km. Auroral detections shown in Figure 2 (top panel) are comparable to those of Schneider21. The number of auroral detections is quite different though: Schneider21 detects additional auroral events because the authors sum up the spectra and thus obtain a higher SNR, while our study used individual spectra to retrieve limb profiles.

3. Spectral Study

The aim of this section is to estimate the intensities of the auroral emissions. Only those spectra when both the CO Cameron and CO_2^+ UVD brightness exceeded a 1-σ uncertainty level were considered. This cutoff leads to the removal of many spectra, mainly because of the CO_2^+ UVD emission that is generally fainter

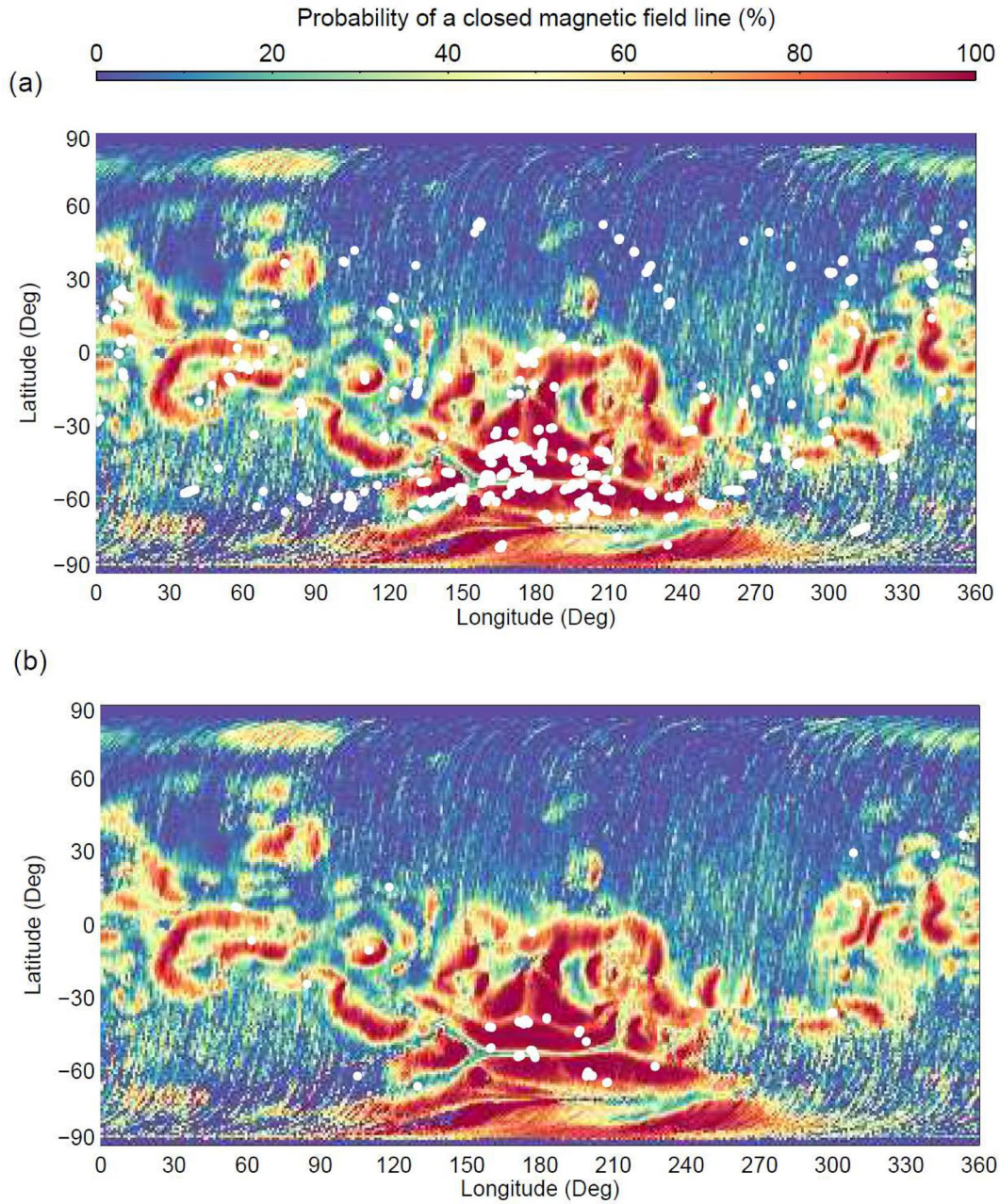

Figure 2. (a) Locations of the tangent altitude points of Mars Atmosphere and Volatile EvolutioN/Imaging UltraViolet Spectrograph (MAVEN/IUVS) auroral limb detections are shown with white dots. They are overlaid on top of the statistical map of probability of open/closed magnetic field lines from the Mars Global Surveyor (MGS) measurements. (b) Same for the weaker, and thus less numerous, 297.2 nm [OI] detections.

and has a lower signal-to-noise ratio than the Cameron emission. A total of 1,246 spectra matched this criterion.

3.1. MUV Emissions

First, all selected spectra have been averaged to generate the mean discrete auroral spectrum shown in Figure 3. Several spectral features can be identified: the CO ($a^3\Pi$-$X^1\Sigma$) Cameron bands between 190 and 270 nm, the CO_2^+ ($B^2\Sigma_u^+$-$X^2\Pi_g$) UVD at 288–289 nm and the [OI] at 297.2 nm forbidden line. For the first

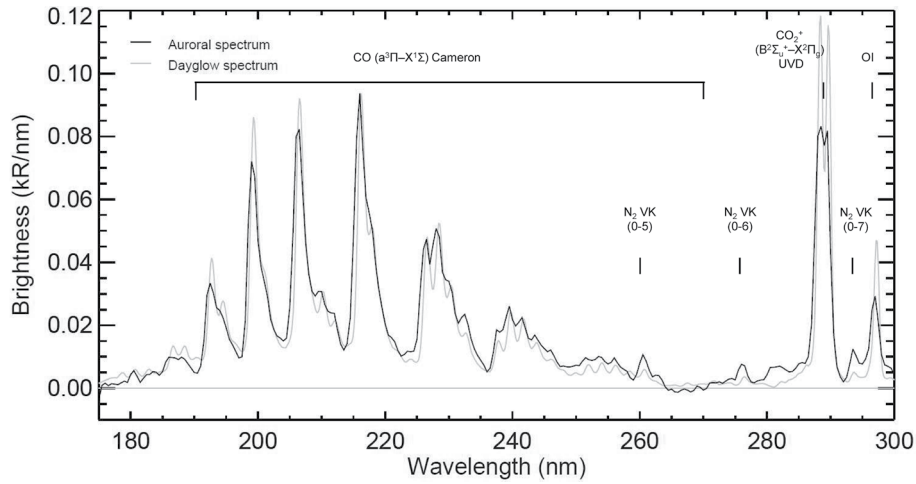

Figure 3. The averaged spectrum of the MUV IUVS auroral detections (black line). A Mars Atmosphere and Volatile EvolutioN/Imaging UltraViolet Spectrograph (MAVEN- IUVS) dayglow spectrum (Gérard et al., 2019), whose intensities have been normalized to the strongest CO Cameron emission band, is plotted in gray for comparison.

time in the Martian aurora, we also detect the (0–5), (0–6), and (0–7) bands of the N_2 Vegard-Kaplan (VK) bands at 260.4, 276.1, and 293.7 nm.

The Martian dayglow spectrum has been plotted in gray for comparison. The dayglow spectrum has been divided by 140.5 to normalize the strongest CO Cameron emission band to that of the auroral spectrum. The shapes of both spectra are almost identical, suggesting that similar dominant processes and source species are involved on the dayside and the aurora. The CO_2^+ UVD and [OI] emissions appear to be relatively brighter than the CO Cameron emission in the dayglow spectrum, while the N_2 VK are more easily identified in the auroral spectrum.

The N_2 VK bands are too weak to make a statistical study of their brightness. However, in the following sections, the CO Cameron, CO_2^+ UVD, and [OI] emissions will be analyzed in detail.

3.2. Emissions Analysis

3.2.1. CO Cameron and CO_2^+ UVD Emissions

Peak altitudes and intensities of the CO Cameron and CO_2^+ UVD emissions have been derived from cleaned L1C spectra. Intensities in these spectra were obtained by fitting a synthetic spectrum of the corresponding emission to the observed spectrum. Additional information about the retrieval of the emission intensities can be found in Schneider21. Peak altitudes are derived from limb profiles, as shown in Figures 1c and 1d. These limb profiles have been generated by using the seven spatial bins along the slit of the image detector (Figure 1a) that have been acquired at different altitudes of the atmosphere owing to the slight tilt of the slit relative to the horizon. Because each detector image is composed of seven spatial bins, the limb profiles are made of seven data points. Figure 1c shows a limb profile of the CO_2^+ UVD emission while Figure 1d shows a profile of the CO Cameron emission. The point corresponding to the spectrum shown with the red rectangle in Figure 1a is represented with a red plus symbol on the generated limb profile. For each of the limb profiles considered, the altitude and the brightness of the peak emission have been extracted, together with their coordinates at the tangent point (latitude, longitude, solar longitude, local time, etc.).

We first focus on the peak intensities of the CO Cameron and CO_2^+ UV doublet emissions. Only limb profiles showing a clear peak with an intensity brighter than the 1-σ uncertainty level were retained for this study. Figures 4a and 4b show a latitude-longitude map of the color-coded peak intensities of the CO Cameron and CO_2^+ UVD emissions. The mean intensities are 1.6 and 0.23 kR, respectively. As also demonstrated in Schneider21, highest intensities occur in the most structured magnetic field area.

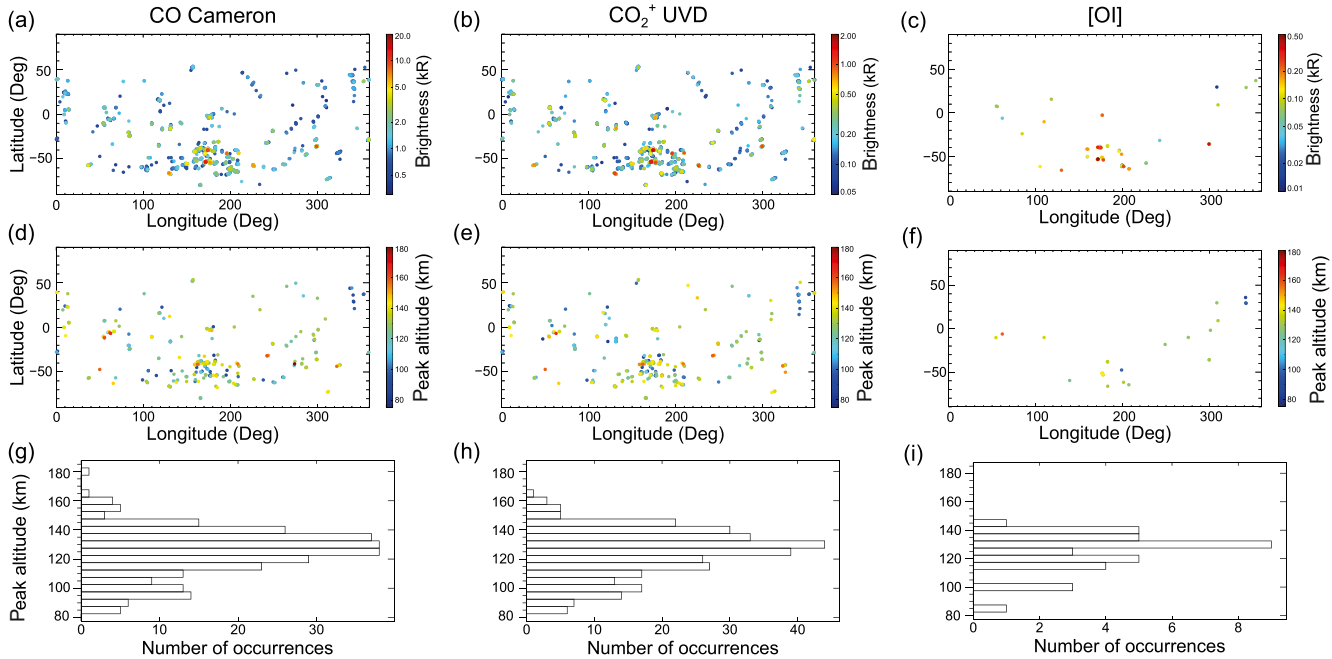

Figure 4. Locations and intensities of the CO Cameron (a), CO_2^+ UVD (b), and [OI] (c) auroral emissions. Locations and peak altitudes of the CO Cameron (d), CO_2^+ UVD (e), and [OI] (f) auroral emissions. Distribution of the peak altitudes of the CO Cameron (g), CO_2^+ UVD (h), and [OI] (i) auroral emissions.

Figures 4d and 4e are similar to the previous panels but they represent the peak altitudes of the CO Cameron and CO_2^+ UVD emissions. No correlation is observed between the altitude of the discrete aurora and its location. The distributions of the peak altitudes are shown with histograms in Figures 4g and 4h. Both distributions are very similar and they peak at a tangent altitude of 130 km, with a mean value of 124.4 km ± 17 km for the CO Cameron emission, within the limb viewing SPICAM determination range of 137 km ± 27 km (Soret et al., 2015). Peak altitudes have been observed from ~80 to ~180 km. However, individual limb observations do not generally cover this wide range of altitudes (see Figures 1c and 1d). It is thus possible that the retrieved peak altitude does not correspond to the brightest auroral emission altitude, that might be located below or above the atmospheric layer that has been observed by IUVS. Also note that the spread of the peak altitude distributions is not only a measurement of its true variability but a consequence of the projection effects for the emission patches that are not necessarily located at the altitude of their tangent point: they may also be located either in the foreground or the background of the tangent point along the line-of-sight. Thus, observed altitudes can be lower than where aurorae actually occur. This geometric effect is explained in detail in Schneider21. The large amount of data used to generate these statistics indicates that the auroral layer generally occurs at ~130 km.

3.2.2. Correlations Between the CO Cameron and CO_2^+ UVD Emissions

We now analyze the correlation between the CO Cameron and CO_2^+ UVD brightnesses and their peak altitudes. To do so, each of the individual spectra acquired by the IUVS instrument and showing an auroral feature has been used. Figure 5a shows the emission ratio for the CO Cameron and CO_2^+ UVD emissions (from Figures 4a and 4b), which can be a diagnostic for excitation and emission mechanisms and/or radiative transfer of the emitted light. It shows a clear correlation between the CO Cameron and the CO_2^+ UVD intensities. The same trend is also observed when specifically considering the intensities at the peak of the emission (not shown here). The solid line represents the least mean squares linear fit to the data set. It shows that the CO Cameron brightness is statistically 6.6 ± 0.1 times brighter than the CO_2^+ UVD. The dashed lines indicate the mean values of 1.6 and 0.23 kR for the CO Cameron and the CO_2^+ UVD intensities, respectively. This ratio is within the range of the auroral ratios determined with the SPICAM instrument on board Mars Express. Gérard et al. (2015) found a mean ratio of 4.9 for nadir observations and Soret et al. (2015) obtained a mean ratio of 9.0 for the limb observations. This ratio is also relatively close to previously calculated and observed ratios in the dayglow. Shematovich et al. (2008) found a ratio of 6.7 from a

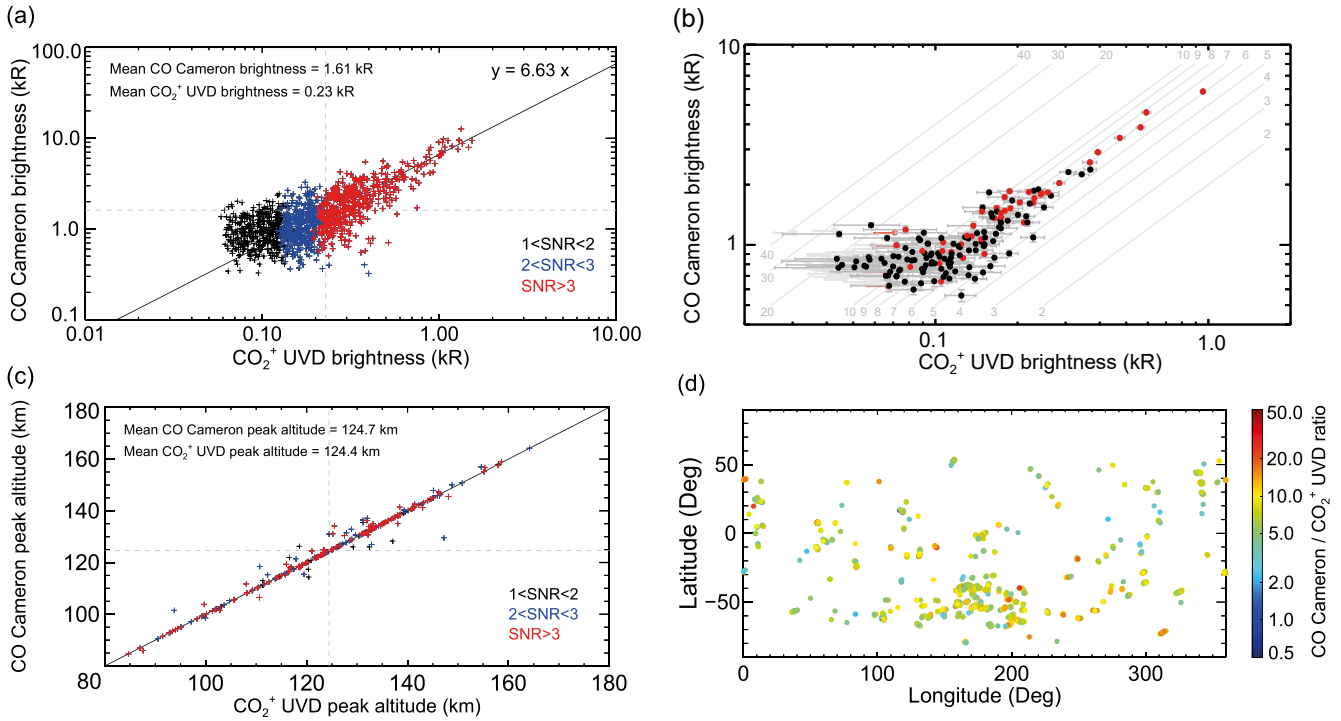

Figure 5. (a) Variation of the CO Cameron and CO_2^+ UVD discrete auroral emissions intensities extracted from individual spectra. The solid line is the best fit through the data points. The color of the data points depends on the value of the combined CO Cameron and CO_2^+ UVD signal-to-noise ratio (SNR), mostly controlled by the fainter CO_2^+ UVD emission. Note the logarithmic scale. (b) Brightness ratio of the CO Cameron band versus CO_2^+ UVD. Red dots indicate detections in the strong crustal field region, 1-σ uncertainties are shown. Gray dots with arrows indicate 3-σ upper limits and diagonal gray lines indicate lines of constant emission ratio. (c) Correlation between the altitude of the CO Cameron and CO_2^+ UVD emission layers. (d) Locations and brightness ratio of the CO Cameron and CO_2^+ UVD auroral emission intensities.

limited sample. Cox et al. (2010) observed the Mars dayglow with the SPICAM instrument and deduced a ratio of 4.7. Stiepen et al. (2015) analyzed a larger SPICAM data set and derived a Cameron/CO_2^+ UVD ratio of 5.2. Gérard et al. (2019) analyzed MUV dayglow spectra acquired by MAVEN-IUVS and obtained ratios ranging from 4.7 to 5.7. This suggests that even though the excitation processes are partly different, they produce rather similar dayglow and discrete auroral spectra.

Figure 5b includes all summed-up auroral detections for which the signal-to-noise ratio is >3 as described in Schneider21. The 3-σ upper limits are shown in gray for the 40% of auroral detections for which UVD emission was not observed. The brightest emissions, preferentially from the strong crustal field regions (in red), cluster fairly closely around the ratio value of 7. The spread becomes broader at lower signal levels, but it cannot be completely attributed to increased noise levels. Statistically significant outliers lie both above and below the ratio of 7 line, with a large number of outliers for higher values of the ratio where brighter CO Cameron emissions occur with dimmer CO_2^+ emissions. A possible explanation for these high ratio values will be given in Section 4.3.2.

The peak altitude of the CO Cameron emission (from Figure 4d) as a function of that of the CO_2^+ UVD (from Figure 4e) is shown in Figure 5c. The statistical distribution of data points along the bisector clearly demonstrates that the two emissions always peak very close to the same altitude, even though the altitude of the tangent point ranges from 80 to 160 km. Note again that the tangent altitude does not necessarily represent the actual location of the aurora: it would be located at higher altitudes if observed in the foreground or the background along the line-of-sight. The dashed lines indicate a mean altitude of 124.7 ± 1.0 and 124.4 ± 1.0 km for the CO Cameron and the CO_2^+ UVD emissions, respectively. These values are slightly different than in the dayglow where Shematovich et al. (2008), Cox et al. (2010), Gérard et al. (2019), and González-Galindo et al. (2021) all concluded that the CO Cameron layer is located a few kilometers above the CO_2^+ UVD layer (~121 and ~119 km, respectively). This offset stems from the different dominant

sources of the Cameron bands in the dayglow and the aurora. In the aurora, the main source of both the UV doublet and the Cameron bands is electron impact on ground state CO_2 molecules, which creates emission peaks at the same altitudes. In contrast, the production of CO_2^+ UVD in the dayglow is dominated by photoionization of CO_2 into the $B^2\Pi_u$ state that peaks 2–3 km higher than the electron source (Gérard et al., 2019). Note also that no relation could be found between the brightness and the altitude of the peak emissions.

The latitude-longitude map of the CO Cameron/CO_2^+ UVD ratio presented in Figure 5d does not show any trend, implying that the ratio does not depend on the location of the discrete aurora nor the presence of a crustal magnetic field (see also Section 3.3.2).

3.2.3. [OI] Emission at 297.2 nm

The forbidden [OI] emission at 297.2 nm has also been detected in the discrete auroral limb spectra (see Figure 3), but not in all of them, due to the low brightness of this emission and the lower sensitivity of the IUVS detector at this wavelength. Considering the full 1,246 spectra data set described above, the mean [OI] brightness is 34 R. This value leads to CO Cameron/[OI] and CO_2^+ UVD/[OI] ratios of 47.6 and 6.8, respectively. However, another selection of the spectra to be used in this section was performed. Only spectra showing unambiguous emission at 297.2 nm with a brightness greater than the 1-σ uncertainty level were retained, reducing the database to 62 spectra. The location and intensities of the [OI] emission can be seen at the bottom of Figure 2b and in Figure 4c. The mean value of the detected [OI] emission is 140 R. As for the other emissions, the brightest emissions appear to occur in the strong magnetic field region.

Figure 4f shows the peak altitude of the [OI] emission on a latitude-longitude map while the distribution of the peak altitude is shown with a histogram in Figure 4i. The histogram distribution peaks at 130 km and the mean peak altitude value is 128.2 ± 3.3 km, a value consistent with the altitude layer of the CO Cameron and CO_2^+ UVD emissions.

No linear trend has been found between the [OI] brightness and those of the CO Cameron bands or the CO_2^+ UVD emissions. This could be a consequence of the production mechanisms involving electron impact on O and CO while CO_2 is the main source of CO Cameron and CO_2^+ UVD emissions (Gérard et al., 2017). However, this is unlikely since CO_2 is the most abundant constituent of the atmosphere at the altitude of the [OI] emission. Nevertheless, in the case of concurrent observations, we find mean ratios of CO Cameron/[OI] of 26.1 and CO_2^+ UVD/[OI] of 3.7.

3.2.4. N_2 Vegard-Kaplan Band Emissions

The (0, 5) and (0, 6) VK bands were first observed in SPICAM dayglow spectra by Leblanc et al. (2006). Their presence was confirmed by Stevens et al. (2015) who obtained IUVS limb profiles following careful subtraction of other spectral components, including solar scattered light. The total emission between 258 and 288 nm reached a peak brightness of 3 kR at 125 km. In the MAVEN/IUVS dayglow spectrum shown in Figure 3, the N_2 VK (0, 5), (0, 6), and (0, 7) emissions are 410, 312, and 185 R, respectively.

In this study, N_2 VK bands cannot be detected in individual spectra owing to their low intensities. However, because of a higher signal-to-noise ratio following addition of more than a thousand spectra and the lack of solar radiation background, the VK (0, 5), (0, 6), and (0, 7) at 260.4, 276.1, and 293.7 nm, respectively, have been detected for the first time in the Mars aurora. They can be seen in the averaged spectrum of Figure 3. We estimate the N_2 VK (0, 5), (0, 6), and (0, 7) emissions to be 6.8, 5.9, and 7.2 R, respectively. This implies that the VK (0, 5), (0, 6), and (0, 7) bands are about 60, 53, and 26 times brighter in the dayglow than in the aurora, respectively. The CO Cameron ratio with the total of the VK (0, 5), (0, 6), and (0, 7) emissions in the aurora is 80, while this ratio is 248 for the dayglow. The CO Cameron/N_2 VK in the aurora is thus a factor of 3.1 greater than the ratio on the dayside. Jain and Bhardwaj (2011) explained that the VK dayglow emission is highly dependent on the N_2/CO_2 ratio. It could explain the CO Cameron/N_2 VK ratio difference observed in the dayglow and the aurora.

The CO_2^+ UVD ratios with the VK (0, 5), (0, 6), and (0, 7) emissions in the aurora are 34, 39, and 31, respectively.

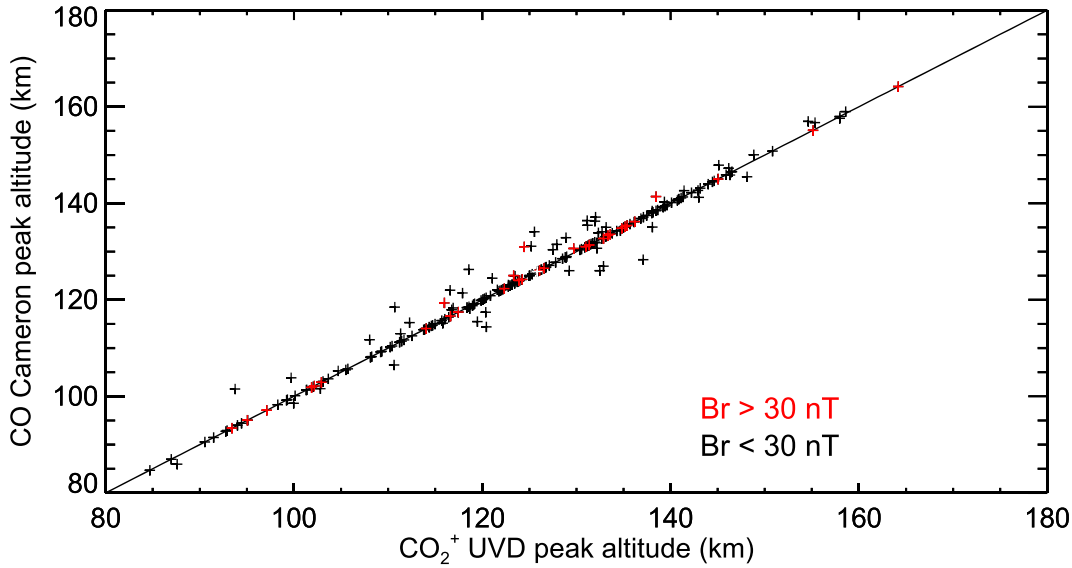

Figure 6. Correlation between the peak altitude of the CO Cameron and CO_2^+ UVD emissions. Observations made where the radial component of the crustal magnetic field is greater than 30 nT are plotted in red while observations made where the radial component is smaller than this value are plotted in black. The altitude of the emission layer is independent of the presence or absence of a crustal magnetic field.

3.3. Influence of External Parameters

3.3.1. Local Time Variations

Schneider21 shows that aurorae are more frequent during the evening hours, especially before 22 h local time. We have analyzed the variations of their altitude with local time but could not find any correlation. Whatever the local time, the peak altitude of the CO Cameron emission consistently remains overall stable at ~125 km. Thus, it appears that some mechanism favors the appearance of discrete aurora during the evening hours but do not impact the characteristics of the discrete aurora itself.

3.3.2. Crustal Magnetic Field Area

We now examine whether the presence or absence of a structured magnetic field exerts any influence on the altitude of discrete auroral emissions. Such an effect would be an indication that the mean auroral electron energy is different in the two regions, a possible suggestion that the acceleration processes act differently. Schneider21 shows that the Cameron and CO_2^+ UVD intensities are statistically stronger in regions with strong radial magnetic field area. A threshold of Br = 30 nT is suggested, where Br is the average radial magnetic field measured by the MAVEN-MAG magnetometer below 250 km altitude (Weber, 2020). We thus divide the IUVS auroral events into two subcategories: the first data set includes the auroral detections acquired in strong radial magnetic field area (Br > 30 nT), while the second data set considers aurorae collected where the magnetic field is low (Br < 30 nT). In Figure 6, red plus symbols correspond to observations acquired in strong radial magnetic field areas while black dots have been observed outside of it. The distribution of the tangent altitudes of the CO Cameron emission is almost identical in both areas, ranging from ~90 to ~160 km, and their average value closely corresponds to the same altitude (125.3 ± 2.8 km and 124.2 ± 1.4 km, respectively). We conclude that the peak altitude distributions of the Cameron and the CO_2^+ UVD emissions are statistically identical, no matter the radial component of the crustal magnetic field.

Thus, the magnetic field structure does not influence the altitude of the discrete auroral emission. Schneider21, however, notes that aurorae tend to be observed more frequently in the magnetic field area than outside of it and that the CO Cameron intensities (and, since they covary, also the CO_2^+ UVD brightness) are larger when the field strengths exceed 30 nT below 250 km.

This result is somewhat counter intuitive. The presence of the crustal magnetic field causes mirroring and increases the number of backscattered electrons. In the case of an isotropic pitch angle distribution, the

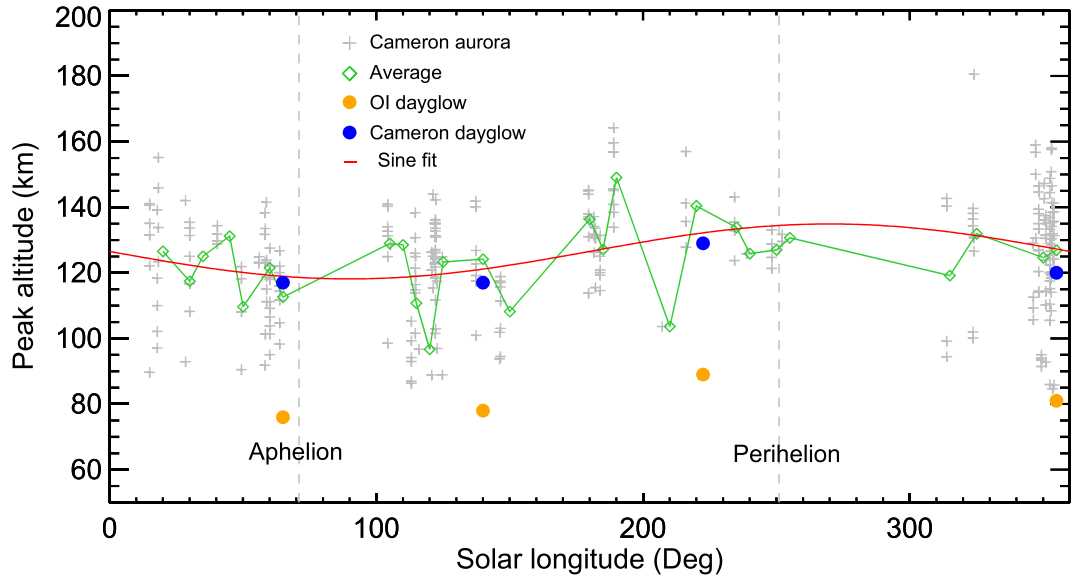

Figure 7. Seasonal variation of the peak altitude of the CO Cameron discrete auroral emission (+) and binned values (◊). The red line is a sine fit through the data. The brown and blue dots show the seasonal variation of the dayglow altitude.

convergence of the magnetic field lines compensates the loss by the mirrored population so that the total flux is conserved. One-dimensional simulations with the Monte-Carlo electron transport model by Bisikalo et al. (2017) indicated that the backscattered population increases by up to a factor of 3 at 400 eV in the presence of a crustal magnetic field of 23 nT at 100 km. A higher statistical number of auroral detections and increased auroral brightness are observed in the crustal field region. We suggest that the number flux of auroral electrons increases in areas with B field intensity exceeding 30 nT below 250 km, while leaving the mean electron energy almost unaffected. This interpretation is in agreement with the results described in Section 3.3.2 showing that the altitude distribution of the ultraviolet emissions is similar inside and outside the strong crustal field regions. The complex interplay between magnetic mirror force, convergence of the magnetic field lines, pitch angle distribution, collisional scattering, and possible presence of a field-aligned electric field may result in an increase of the ionization rate and auroral emissions in strong magnetic field regions (Lillis & Fang, 2015).

3.3.3. Seasonal Variations

In this section, we focus on the variations possibly associated with seasonal effects. The peak altitudes of the detected discrete aurorae are represented in Figure 7 with gray plus signs. They have then been grouped into 5° solar longitude bins, which are plotted with green diamonds and linked together by a green solid line. A sine fit of the peak altitudes is overplotted in red. The minimum of the peak altitude of the discrete auroral layer appears to occur near aphelion while its maximum is observed near perihelion. It clearly shows that the variations of the altitude of the discrete auroral emission could be caused by seasonal effects. For comparison, altitudes of the [OI] and CO Cameron layers observed in the Martian dayglow are shown by orange and blue dots (Gérard et al., 2019). Their study showed that this seasonal variation is explained by an expansion of the Martian atmosphere in the vicinity of perihelion, causing the thermospheric temperature to increase and the pressure levels to move up. It is thus likely that the emission peak of the discrete aurora is produced when precipitating electrons reach a given pressure level, whose altitude varies with the season. Assuming that the mean energy of the precipitating electrons is statistically constant over the Martian year, this would imply that the atmospheric structure induces this variation.

No clear conclusion can be reached about the variations of the auroral brightness with seasons, but no dependence between the brightness and the solar longitude is theoretically expected. Indeed, the auroral production mechanisms occur at different altitude layers depending on season, but this does not affect the brightness of the emission at the altitude of the given pressure level.

4. Electron Precipitation: Relation With UV Aurora

4.1. SWEA Measurements

It is expected that strong electron precipitation events correlate with discrete auroral event detections following the interaction of energetic electrons with CO_2 in the upper atmosphere. The main sources for Cameron bands and CO_2^+ UVD are:

$$CO_2 + e\left(E > 11.5\,eV\right) \rightarrow CO\left(a^3\prod\right) + O + e, \quad (1)$$

$$CO_2 + e\left(E > 18.1\,eV\right) \rightarrow CO_2^+\left(B^2\Sigma\right) + e + e, \quad (2)$$

while a minor source for the production of the CO Cameron bands is:

$$CO + e\left(E > 6\,eV\right) \rightarrow CO\left(a^3\prod\right) + e. \quad (3)$$

Leblanc et al. (2008) first examined the possible correlation between discrete auroral detection with electron precipitation using SPICAM data. They compared the auroral events with simultaneous measurements of energetic electron of the Analyzer of Space Plasmas and EneRgetic Atoms (ASPERA-3) and the Mars Advanced Radar for Subsurface and Ionosphere Sounding (MARSIS) total electron content measurements. They deduced that a correlation appears to exist between the occurrences of both events. However, no clear correlation was found between the intensity of the incident electron flux and the total electron content or the auroral emission intensities. Gérard et al. (2015) also compared the UV auroral detections at the nadir from the entire SPICAM database with concurrent ASPERA-3 measurements and determined the characteristics of the electron energy spectra at the time of the most-likely associated electron flux enhancements. However, although SPICAM was then observing in the nadir direction and detected auroral events associated with energy flux enhancements, they did not find a clear linear correlation between the observed brightness and the concurrent precipitated electron energy flux.

In this study, we use MAVEN Solar Wind Electron Analyzer (SWEA; Mitchell et al., 2016) measurements to study correlations between electron precipitation events and the presence of discrete aurorae. SWEA is a symmetric hemispheric electrostatic analyzer with deflectors. It measures the energy and angular distribution of electrons with energies between 3 and 4,600 eV in 64 logarithmically spaced energy bins. The instrument reaches an energy resolution of 17% ($\Delta E/E$). The field of view is divided into 16 azimuth and six elevation angles. It is mounted on 1.5 m boom on the MAVEN spacecraft allowing an 80% field of view of the sky for energies up to 2,000 eV, while for higher energies the field of view decreases. Since SWEA acquires the energy of the precipitating flux versus time, these data can be analyzed at the time of discrete auroral detections (see Figure 8). For this study, we use omni-directional electron energy spectra available from NASA PDS in units of differential energy flux (eV/cm^2 s sr eV) with a temporal resolution of 2 s. Considering the minimum electron energies necessary for the excitation of the Cameron bands and CO_2^+ UVD, only electron energies above 10 eV are used for this analysis. The integrated flux above 10 eV shown in Figure 8 is additionally converted into units of W m^{-2} s^{-1}.

We focus on six discrete auroral events and compare them with SWEA measurements. For completeness, these auroral events have been selected with as much diversity as possible:

1. Auroral events detected during orbit 3520 occur above a magnetic field area (longitude ∼50°, latitude ∼−10°S) but not the most structured one of the southern hemisphere.
2. Auroral events from orbits 8615, 8627 (see Figures 1 and 8) and 8687 occur in the "valleys" of the strongest crustal magnetic field region.
3. Auroral events from orbit 8675 are very bright and have been observed between the very southern region of the strong magnetic field area and the equator.
4. Auroral events from orbit 9460 have been detected outside the magnetic field area and show a very strong CO_2^+ UVD emission.

Each of these orbits will be described hereafter and summarized in Table 1. However, it is important to note that the SWEA and the IUVS observations are concurrent in time but not spatially coincident. The SWEA measurements are made at the spacecraft position, while the detected auroral events occur somewhere along the line-of-sight of the limb observation, at the tangent point altitude or above.

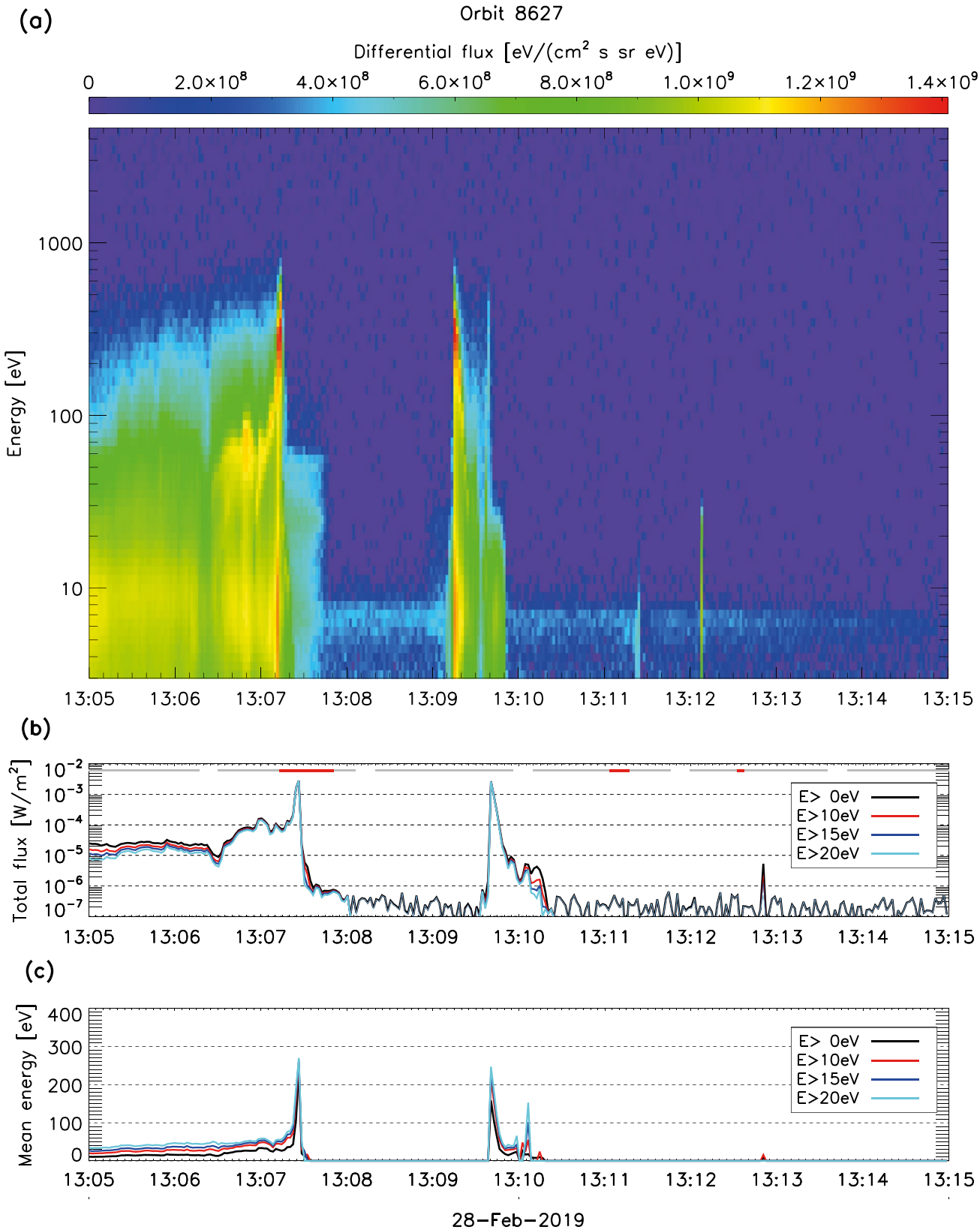

Figure 8. (a) Differential electron energy flux measured by SWEA along orbit 8627; (b) Integrated energy flux above 10, 15, and 20 eV; (c) Mean energy of the precipitating electrons deduced from the observations derived from panel (a). In panel (b), gray lines at the top indicate MAVEN/IUVS concurrent observations. Red lines indicate that a discrete aurora has been observed at that time.

Table 1
Concurrent Imaging UltraViolet Spectrograph (IUVS) Auroral Detections and SWEA Electron Integrated Flux

MAVEN-IUVS					MAVEN-SWEA			Model
Orbit	UTC	CO Cameron brightness (kR)	Altitude of the tangent point (km)	MAVEN tangent point distance (km)	UTC	Integrated electron flux (mW/m^2)	Mean energy >10 eV (eV)	Predicted electron energy (eV)
3520	11:02:12	1.8	156	261	11:02:12	1.1	116	<10
8615	11:08:28	1.7	131	381	11:07:27	2.2×10^{-3}	31	208
8627	13:11:03	4.1	145	532	13:09:40	2.7	216	18
8675	18:09:14	3.5	110	451[a]	18:08:05	0.23	68	1,332
8687	18:27:13	9.4	132	293	18:27:07	0.24	66	185
9460	13:10:58	3.8	118	547	13:10:59	1.4×10^{-4}	<0.1	885

[a]Schneider21 estimates the actual distance to be 692 km (see text).

4.2. Correlation With Auroral Events

We discuss here the possible correlations between precipitating electrons event measured by SWEA and aurora detections by IUVS for each orbit.

4.2.1. Orbit 3520

Auroral events were observed by IUVS at 11:00 and 11:02 UTC (red horizontal lines on top of Figure 9a). The most prominent feature in the SWEA measurements is observed at 10:57:05 when no auroral detection were found (gray horizontal lines on top of Figure 9a). In contrast, the auroral event occurring at 11:00 shows a significantly smaller increase of the integrated flux in the corresponding SWEA measurements. Because the spacecraft was located ~635 km away from the limb tangent point, the distance between the location of the electron precipitation measurements and that of the aurora could explain the apparent inconsistency. At 11:02, however, the locations of MAVEN and the tangent point of the auroral emission are almost coincident (~260 km apart) and both an auroral event and an increase in the integrated flux (up to 1.1 mW/m^2) are observed at the exact same time.

4.2.2. Orbit 8615

Aurorae are observed at 11:03, 11:05, and 11:08 UTC with IUVS. In the SWEA energy flux (Figure 9b), an inverted-V shape (Brain et al., 2006) is observed at 11:01:57. Inverted-V electron acceleration events are characterized by an enhanced flux in a narrow energy band and are responsible for discrete auroral emissions on Earth. However, the distance of ~1,100 km between the spacecraft and the tangent point does not guarantee that the aurora observed at 11:03 actually took place at the location of the SWEA acquisition.

An auroral event has been detected between 11:05 and 11:06 but there is a clear minimum in the SWEA measurements at that time. Once again, the spacecraft is located ~1,000 km away from the tangent point and the observed SWEA energy flux might not be related to the auroral event. Two strong integrated fluxes are then observed at 11:05:49 and 11:06:47. They have been extensively analyzed by Xu et al. (2020). Unfortunately, no auroral event was detected at those times.

At 11:08, the spacecraft and the tangent point are almost coincident (~380 km apart). Yet, the SWEA integrated flux measured at that time is very weak (2.2×10^{-3} mW/m^2) and should not give rise to a measurable auroral emission. It thus appears that the observed discrete aurora is not generated by this flux of energetic electrons.

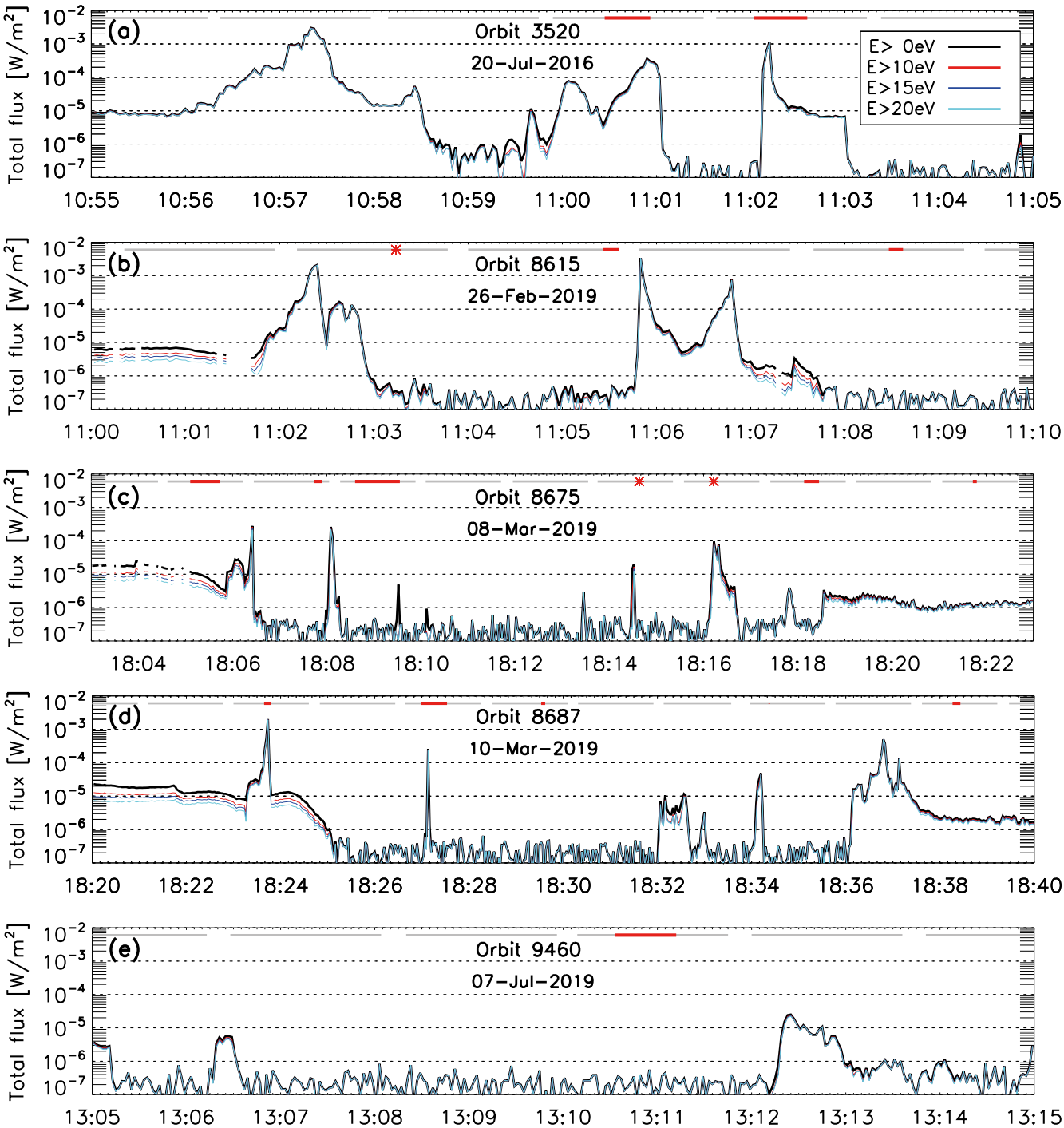

Figure 9. Same as Figure 8b for orbits 3520 (a), 8615 (b), 8675 (c), 8687 (d), and 9460 (e). Gray horizontal lines at the top indicate Mars Atmosphere and Volatile EvolutioN/Imaging UltraViolet Spectrograph (MAVEN/IUVS) concurrent observations. Red lines indicate that auroral events lasting several seconds have been observed at that time while red stars represent a single detection in one spectrum.

4.2.3. Orbit 8627

The SWEA measurements (Figure 8) present two bright inverted-V shapes at 13:07:20 and 13:09:40, with a very low integrated flux in between. Auroral events have been detected at 13:07 (tangent point located ~1,130 km from the spacecraft), 13:11 (~530 km away from the spacecraft; see also Figure 1) and 13:12

(~325 km away from the spacecraft). In this configuration, the 13:11 auroral detection and the 13:09:55 electron precipitation event are probably related.

4.2.4. Orbit 8675

The integrated flux shown in Figure 9c peaks at 18:06:15 and 18:08:05. Two other moderate integrated fluxes are detected at 18:14:31 and 18:16:13. Several auroral events have been detected during orbit 8675: at 18:05 (tangent point ~835 km away from the spacecraft), 18:07 (~740 km away from the spacecraft), 18:09 (tangent point and spacecraft are located ~450 km apart), 18:14 (~410 km between the tangent point and the spacecraft), 18:16 (~565 km away), 18:18 (~820 km away), and 18:22 (~1,390 km apart). Schneider21 actually tries to determine the real location of the aurora along the line of sight for this specific orbit. The authors deduce that the tangent point is a good approximation of the actual location of the 18:05 aurora. The 18:06 is more likely to occur ~147 km away from the MAVEN spacecraft while at 18:09, the auroral emission is expected to occur in the background of the tangent point (~692 km away from the spacecraft).

Anyway, the 18:09 auroral detections and the 18:08:05 SWEA event are most certainly related. The single IUVS spectrum acquired at 18:14 matches the SWEA integrated flux at the same time even though it is a very low precipitating electron flux (1.2×10^{-2} mW/m^2). Note also that MAVEN is almost coincident with the limb tangent point at that time. Other events are too far apart to be coincident.

4.2.5. Orbit 8687

Aurorae have been detected at 18:23 (~830 km away from the spacecraft), 18:27 (~290 km), 18:29 (~525 km apart) and for a very short moment at 18:34 (~710 km apart), and 18:38 (~1,140 km apart). We can confidently claim that the 18:27 auroral event is due to the electron precipitation whose integrated flux reached 0.24 mW m^{-2} at that time (Figure 9d).

4.2.6. Orbit 9460

An auroral event occurred at 13:10 (~550 km away from the spacecraft) during orbit 9460 and no measurement can explain this auroral event in the SWEA electron precipitation of Figure 9e. Note that for this orbit, MAVEN (and therefore the SWEA measurements) was flying above a region without any structured magnetic field.

Table 1 summarizes the times of these observations and lists the characteristics of the IUVS and SWEA auroral detections. Overall, it seems quite difficult to associate a given auroral event to a specific burst of electrons event: either the SWEA measurement is not made at the location of the aurora or the integrated electron flux is too weak to explain the presence of the aurora. This lack of correlation was already observed by Gérard et al. (2015) between SPICAM and ASPERA-3 measurements. They explained that the auroral emission may be shifted from the enhanced electron flux because the field lines threading the electron events are probably tilted from the vertical. Another difficulty is that if the SWEA measurements are made very close to the tangent point of the limb observations, the distance is too short to cover a full range of altitudes through the atmosphere. In this case, we can determine whether auroral and precipitating electrons events are correlated, but we lose information about the altitude of the aurora.

4.3. Monte-Carlo Simulations

4.3.1. Model Description

IUVS auroral brightness measurements can also be compared with numerical simulations based on the SWEA measurements. In this study, we use the same electron transport model as Soret et al. (2015) which is based on a direct-simulation Monte-Carlo (DSMC) method to solve the Boltzmann kinetic equation. The details of the numerical model have been described earlier (Shematovich et al., 1994, 2008). The evolution of the system of test particles is calculated from the initial to the steady state. The application of the model to the Mars dayglow and aurora was described by Gérard et al. (2015, 2017) and applied to the discrete and diffuse aurora. The lower boundary is located at altitude 50 km and the upper boundary is set at 300 km. The electron pitch angle distribution at the top of the model is isotropic over one hemisphere. The list of

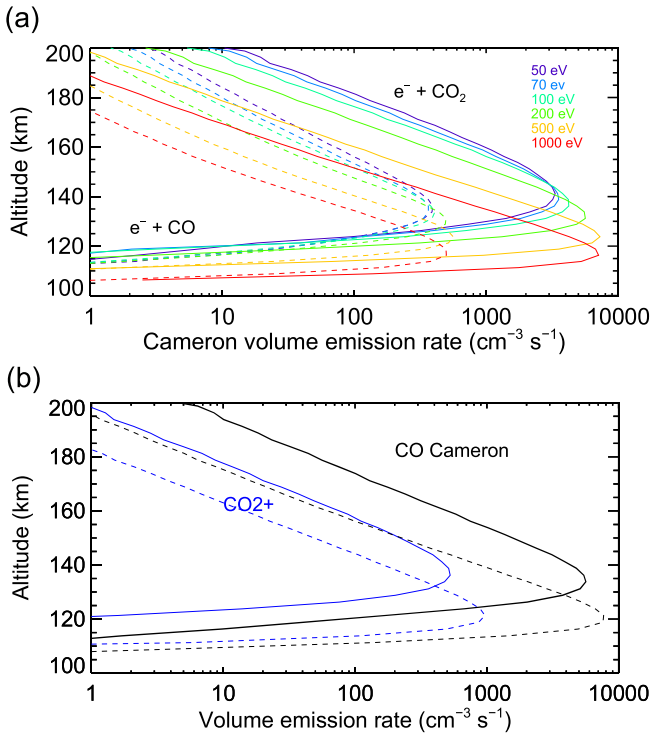

Figure 10. (a) Volume emission rates of the CO Cameron emissions for several monoenergetic electron precipitations carrying an energy flux of 1 mW/m^2. Solid lines represent process (1) while dashed lines represent process (3). (b) Vertical profiles of the total CO Cameron emission (black lines) and CO_2^+ UVD emission (blue lines) predicted by the model for energies of 150 eV (solid lines) and 700 eV (dashed lines).

cross sections used to calculate energy degradation along the path of the test electrons and further details on the Monte-Carlo model were given by Shematovich et al. (2008).

The CO_2^+ UVD at 288.3 and 289.6 nm from the B $^2\Pi_u \rightarrow$ X $^2\Pi_u$ transition has an excitation threshold of 18.1 eV and the electron impact cross section peaks at 165 eV (Gérard et al., 2019). The CO ($a^3\Pi$) upper state of the Cameron bands is populated by electron impact on CO_2, with a threshold at 11.5 eV, and on CO molecules, with a threshold of 6 eV. The corresponding cross sections for electron impact on CO_2 and CO peak near 80 and 11 eV, respectively. For the e + CO_2 source of the Cameron bands, we use the shape from Shirai et al. (2001) normalized to the value by Erdman and Zipf (1983). We estimate the uncertainty on the absolute cross section to be at least a factor of 2.

As described in Section 3.2.3, the 297.2 nm emission from the O $^1S \rightarrow {}^3P$ transition is also present in the IUVS auroral spectrum. O(^1S) radiative transitions to the ^1D and ^3P levels give rise to the visible green line at 557.7 and the 297.2 nm emission respectively. Simulations of auroral electron impact on CO_2, CO and O producing O(^1S) indicate that collisions with CO_2 dominates over the other two processes. The oxygen 557.7-nm/297.2-nm ratio of Einstein coefficients recommended by NIST is 16.4 (Kramida et al., 2019), and was recently confirmed by Gérard et al. (2020), based on dayglow measurements on Mars from TGO-UVIS.

The CO_2, CO, O, and N_2 density profiles have been calculated with the Mars Global Ionosphere-Thermosphere Model (M-GITM; Bougher et al., 2015). We adopt the density and temperature profiles for local time = 00:00, latitude = 62.5° N, Ls = 270° and F10.7 solar flux index = 160 (at Earth). The corresponding CO_2, CO, and O density profiles were shown in Figure 1 of the diffuse aurora model study by Gérard et al. (2017).

4.3.2. Auroral Emission and Electron Energy

This Monte-Carlo electron transport model calculates the volume emission rates of the emissions forming the auroral signature based on the mean energy of the precipitating electrons. Such profiles are shown in Figure 10a, where the production of the CO Cameron emission by electron impact on CO_2 (process 1 of Section 4.1) and CO (process 3) have been plotted for six cases of monoenergetic electron precipitations of 1 mW/m^2. The production of the CO Cameron auroral emission is dominated by electron impact on CO_2 (process 1). The production of CO_2^+ UVD also results from electron impact on CO_2 (process 2) and vertical profiles of this emission can be seen in Figure 10b (blue lines) for two different energies: 150 eV (solid lines) and 700 eV (dashed lines). The total CO Cameron vertical profiles are represented with black lines. They clearly show that the CO Cameron auroral emission is brighter than the CO_2^+ UVD one, with a ratio ~4.

However, as shown in Figure 5b, large CO Cameron/CO_2^+ UVD ratios have been measured outside the crustal magnetic field region. They are generally associated with low intensities of both emissions. Although these observations are puzzling, a possible explanation is that, for these events, electron impact on CO molecules (process 3) is dominant relative to impact on CO_2. This would imply that, in such circumstances, both processes (1) and (2) make a minor contribution to the excitation of the two emissions, whereas e + CO dominates the Cameron band excitation rate. Two possible scenarios may be envisaged: one where the CO/CO_2 density ratio is unusually large and a second one where the auroral emission is located far from the tangent point and the IUVS line-of-sight only catches the upper part of the aurora where the CO/CO_2 density ratio is larger than at lower altitude. In the model used for these simulations, the CO/CO_2 density ratio is 0.047 at 130 km but increases to 0.95 at 199 km, so that the relative importance of (Equation 3) increases with altitude.

Table 2
Monte-Carlo Discrete Auroral Model Simulations of the CO Cameron Volume Emission Rates for Different Initial Electron Energy Spectra (From Soret et al., 2015)

Energy (eV)	50	70	100	200	500	1,000
Peak altitude (km)	141.2	138.8	136.2	131.2	123.8	116.3
Peak volume emission rate (cm^{-3} s^{-1})	1,433	1,515	1,789	2,375	2,991	2,869

Note. The volume emission rates correspond to an energy flux of 1 mW/m^2.

The peak of the e + CO_2 excitation cross section was determined to reach 2.4×10^{-16} cm^2 at 80 eV by Erdman and Zipf (1983) but several authors have used a value 2–3 times smaller. The e + CO cross section has been re-measured recently as equal to 7.7×10^{-17} cm^2 at 15 eV (Lee et al., 2021). The production rate $P_{B^2\Sigma_u^+}$ of the $B^2\Sigma_u^+$ state is given by:

$$P_{B^2\Sigma_u^+} = n\int_0^\infty \Phi(E)\sigma(E)dE, \quad (4)$$

where n is the CO_2 or CO number density, $\Phi(E)$ is the electron energy spectrum, and $\sigma(E)$ is the excitation cross section of the $B^2\Sigma_u^+$ state for CO_2 or CO. If, for any reason, the CO/CO_2 density ratio increases, the contribution of (Equation 3) relative to (Equations 1 and 2) increases and favors an enhanced Cameron/CO_2^+ UVD brightness ratio.

Model simulations with a Monte-Carlo auroral code shown in Figure 10a indicate that the peak production rate from (a) is only ~14 times higher than by (b) for a monoenergetic precipitation of 500 eV electrons. This ratio decreases with increasing altitude. When considering the entire vertical production column, this ratio drops to ~4.

Table 2 summarizes the characteristics of the total CO Cameron emission peak depending on the electron energy. The more energetic the electrons, the lower they penetrate into the atmosphere (and therefore produce a low-altitude aurora) and the brighter the auroral emission. Also, Soret et al. (2015) showed that the particle flux controls the brightness of the auroral emission but does not modify its altitude.

4.3.3. Model and SWEA Comparison

We can now compare simulations with IUVS observations and SWEA measurements. The altitudes presented in the fourth column of Table 1 are compared to those of Table 2 so that an estimate of the energy of the electrons causing these auroral events can be deduced from the model. These altitudes are those of local volume emissions rates and have not been integrated along the line-of-sight to simulate a limb profile, as discrete aurorae are spatially confined. For this discussion, we assume that aurorae are located in the vicinity of the tangent point. As a comparison, an integration along the line-of-sight would only decrease the peak altitude between 2.5 and 5 km, depending on the mean energy of the electrons considered. It appears that the energies derived from the model do not compare well with the SWEA energy measurements.

For orbit 3520, the observed mean energy is 116 eV while the model predicts that only very low electron energies are needed to produce an aurora at 156 km. Aurorae occurring at that high altitude are somehow very rare though.

The energy calculated by the model for orbit 8615 is about the same order of that measured by SWEA but the measured precipitating electron flux (a few mW/m^2) is much too low to produce any measurable auroral emission. The distance of ~380 km between the SWEA measurement and the IUVS tangent point could explain this discrepancy, especially if magnetic field lines are not aligned in that direction: the measured electron flux is considerably less than the aurora hundreds of kilometers away from it. The same explanation also applies for orbits 8627 and 9460.

SWEA acquisitions for both orbits 8675 and 8687 are almost identical for both the mean energy and the electron flux. However, the IUVS measurements are very different both in altitude and brightness.

The lack of direct correlation between auroral events and electron precipitation events is likely explained by the distance between the two measurements. Also, Gérard et al. (2015) pointed out that magnetic field lines driving the electrons to the atmosphere may be inclined with respect to the vertical direction. This makes quantitative comparisons at the limb even harder to perform.

5. Conclusions

The MAVEN/IUVS limb observations significantly improve the characterization of discrete aurorae on Mars. Owing to the higher sensitivity of the instrument, the number of discrete auroral detections has considerably increased and extended to regions without crustal magnetic field. The high resolution of the instrument also allows us to distinguish many spectral features. As a consequence, the (0–5), (0–6), and (0–7) bands of the N_2 Vegard-Kaplan system have been detected in the MUV auroral spectrum for the very first time. A detailed analysis of the CO ($a^3\Pi$-$X^1\Sigma$) Cameron bands, the CO_2^+ UVD ($B^2\Sigma_u^+$-$X^2\Pi_g$) and the [OI] 297.2 line have been performed. One of the main results of this spectral analysis is that the CO Cameron and the CO_2^+ UVD intensities generally vary linearly, with a ratio of 6.3, except for detections with weak CO_2^+ UVD brightness. This ratio is quite similar to the value observed in the dayglow.

This study also indicates that the peak altitude of the discrete auroral layer is statistically observed at 130 km, for both the CO Cameron and the CO_2^+ UVD emissions. Even if some scatter is observed in the peak altitude layer, we demonstrated that, if both present, the two emissions occur simultaneously at the very same altitude. Moderate seasonal variations of the altitude in the peak emissions have been noticed. The altitude increase observed when Mars approaches perihelion probably results from thermal expansion of the atmosphere.

No statistical difference is observed between the altitude of the peak emissions inside and outside of the crustal magnetic field regions. This somewhat unexpected result raises the question of the acceleration mechanism providing energy to the auroral electrons. It appears that, whatever this acceleration process, it acts similarly on the energy distribution, but not on the energy flux of the electrons in the presence of a magnetic field. The higher statistical brightness in convergent cusp-like crustal magnetic field configurations possibly results from the geometric concentration of the auroral electron flux in regions of converging magnetic field lines rather than increasing the electron mean energy.

In order to understand the relation with the discrete aurora, simultaneous SWEA measurements of electron flux have been analyzed. Even though more orbits may be analyzed, it appears very difficult to quantitatively compare SWEA and IUVS limb detections. This is not straightforward since the position of the SWEA measurements at the spacecraft and the location of the discrete aurora may be quite distant, especially considering that the aurora may be located anywhere along the line-of-sight of the limb observation.

Finally, it would be worth analyzing the FUV region of the IUVS spectra in another study to characterize other auroral emissions such as the CO ($A^1\Pi$-$X^1\Sigma^+$) fourth positive system (CO 4P) and the 130.4 nm OI triplet.

Detection of the [OI] auroral emission at 297.2 nm also raises the question of the observability of emissions beyond 300 nm. The O $^1S \rightarrow {}^1D$ transition produces the transauroral green line at 557.7 nm (ubiquitous in the terrestrial aurora) that is a factor of about 16.5 times brighter than the 297.2 nm line (Gérard et al., 2020; Kramida et al., 2019). The mean observed 297.2 nm limb brightness is about 0.14 kR with a maximum of ~0.4 kR, as shown in Figure 4c. Therefore, the limb brightness of the green line is expected to range from <1 to 7 kR, visible only at the brighter end of the range with the naked eye, but observable with a sensitive detector in the visible. Attempts to detect it with the UltraViolet and Visible Spectrometer instrument on board ESA's Trace Gas Orbiter (NOMAD/UVIS) have failed so far. This nondetection is understandable when considering the low frequency of bright aurorae and the level of the standard deviation of the UVIS background which is estimated to exceed ~1 kR. However, it should be measurable with more sensitive equipment designed for weak airglow observations. The 630 nm line is expected to be much weaker as a consequence of the fast collisional quenching of O(^{1}D) atoms by CO_2.

Another source of visible emission is the CO_2^+ $A^2\Pi_u \rightarrow X^2\Pi_g$ FDB bands extending between ~300 and 500 nm (Lilensten et al., 2015). The electron impact emission cross section is maximum for an incident

electron energy of 165 eV and is a factor of 1.4 higher than the emission cross section for the CO_2^+ UVD (Ajello, 1971). This ratio is also in close agreement with that determined for photoionization of CO_2 by EUV photons of the same energy (Avakyan et al., 1999). We observe CO_2^+ UVD limb brightness up to 1.1 kR (Figure 5a) corresponding to an expected maximum FDB band brightness of about 1.5 kR. Expressed in integrated brightness, this is comparable to the expected green line brightness, but the FDB bands are spread over more than 150 nm. The eye sensitivity for low-level illumination conditions (scotopic vision) peaks near 500 nm but drops by about two orders of magnitude at 400 nm. Consequently, the green line remains the best candidate for naked eye observation by potential future astronauts.

Data Availability Statement

The IUVS and SWEA data may, respectively, be downloaded from the Planetary Atmospheres Node of the Planetary Data System (PDS) at https://pds-ppi.igpp.ucla.edu/search/view/?f=yes&id=pds://PPI/maven.swea.calibrated/data/svy_spec and https://atmos.nmsu.edu/PDS/data/PDS4/MAVEN/iuvs_processed_bundle/l1c/limb/.

Acknowledgments
B. Hubert is a research associate of the Belgian Fund for Scientific Research (FNRS). L. Soret and J.-C. Gérard acknowledge funding from BELSPO, with financial and contractual coordination by the ESA PRODEX Office (PEA Grant No. 4000121493). This study is based partially upon work supported by NASA under award number 80GSFC17M0002. The MAVEN mission is supported by NASA in association with the University of Colorado and NASA's Goddard Space Flight Center.

References

Ajello, J. M. (1971). Emission cross sections of CO_2 by electron impact in the interval 1260–4500 Å. II. *The Journal of Chemical Physics*, *55*(7), 3169–3177. https://doi.org/10.1063/1.1676564

Avakyan, S. V., Ii'In, R. N., Lavrov, V. M., & Ogurtsov, G. N. (1999). *Collision processes and excitation of UV emission from planetary atmospheric gases: A handbook of cross sections*. CRC Press.

Bertaux, J.-L., Korablev, O., Perrier, S., Quémerais, E., Montmessin, F., Leblanc, F., et al. (2006). SPICAM on Mars Express: Observing modes and overview of UV spectrometer data and scientific results. *Journal of Geophysical Research*, *111*, E10S90. https://doi.org/10.1029/2006JE002690

Bertaux, J.-L., Leblanc, F., Witasse, O., Quemerais, E., Lilensten, J., Stern, S. A., et al. (2005). Discovery of an aurora on Mars. *Nature*, *435*, 790–794. https://doi.org/10.1038/nature03603

Bisikalo, V., Shematovich, V., Gérard, J.-C., & Hubert, B. (2017). Influence of the crustal magnetic field on the Mars aurora electron flux and UV brightness. *Icarus*, *282*, 127–135. https://doi.org/10.1016/j.icarus.2016.08.035

Bougher, S. W., Pawlowski, D., Bell, J. M., Nelli, S., McDunn, T., Murphy, J. R., et al. (2015). Mars Global Ionosphere-Thermosphere Model (MGITM): Solar cycle, seasonal, and diurnal variations of the Mars upper atmosphere. *Journal of Geophysical Research: Planets*, *120*, 311–342. https://doi.org/10.1002/2014JE004715

Brain, D., Halekas, J., Peticolas, L., Lin, R., Luhmann, J., Mitchell, D., et al. (2006). On the origin of aurora on Mars. *Geophysical Research Letters*, *33*, L01201. https://doi.org/10.1029/2005GL024782

Brain, D. A., Lillis, R. J., Mitchell, D. L., Halekas, J. S., & Lin, R. P. (2007). Electron pitch angle distributions as indicators of magnetic field topology near Mars. *Journal of Geophysical Research*, *112*, A09201. https://doi.org/10.1029/2007JA012435

Cox, C., Gérard, J. -C., Hubert, B., Bertaux, J.-L., & Bougher, S. W. (2010). Mars ultraviolet dayglow variability: SPICAM observations and comparison with airglow model. *Journal of Geophysical Research*, *115*, E04010. https://doi.org/10.1029/2009JE003504

Deighan, J., Jain, S. K., Chaffin, M. S., Fang, X., Halekas, J. S., Clarke, J. T., et al. (2018). Discovery of a proton aurora at Mars. *Nature Astronomy*, *2*, 802–807. https://doi.org/10.1038/s41550-018-0538-5

Erdman, P. W., & Zipf, E. C. (1983). Electron-impact excitation of the Cameron system ($a^3\pi \rightarrow X^1\Sigma$) of CO. *Planetary and Space Science*, *31*(3), 317–321. https://doi.org/10.1016/0032-0633(83)90082-X

Gérard, J. C., Aoki, S., Willame, Y., Gkouvelis, L., Depiesse, C., Thomas, I. R., et al. (2020). Detection of green line emission in the dayside atmosphere of Mars from NOMAD-TGO observations. *Nature Astronomy*, *4*, 1049–1052. https://doi.org/10.1038/s41550-020-1123-2

Gérard, J.-C., Gkouvelis, L., Ritter, B., Hubert, B., Jain, S. K., & Schneider, N. M. (2019). MAVEN-IUVS Observations of the CO_2^+ UV doublet and CO Cameron bands in the Martian thermosphere: Aeronomy, seasonal, and latitudinal distribution. *Journal of Geophysical Research: Space Physics*, *124*, 5816–5827. https://doi.org/10.1029/2019JA026596

Gérard, J.-C., Soret, L., Libert, L., Lundin, R., Stiepen, A., Radioti, A., & Bertaux, J. L. (2015). Concurrent observations of ultraviolet aurora and energetic electron precipitation with Mars Express. *Journal of Geophysical Research: Space Physics*, *120*, 6749–6765. https://doi.org/10.1002/2015JA021150

Gérard, J.-C., Soret, L., Shematovich, V. I., Bisikalo, D. V., & Bougher, S. W. (2017). The Mars diffuse aurora: A model of ultraviolet and visible emissions. *Icarus*, *288*, 284–294. https://doi.org/10.1016/j.icarus.2017.01.037

González-Galindo, F., Jiménez-Monferrer, S., López-Valverde, M., García-Comas, M., & Forget, F. (2021). On the derivation of thermospheric temperatures from dayglow emissions on Mars. *Icarus*, *358*, 114284. https://doi.org/10.1016/j.icarus.2020.114284

Jain, S. K., & Bhardwaj, A. (2011). Model calculation of N2 Vegard-Kaplan band emissions in Martian dayglow. *Journal of Geophysical Research*, *116*, E07005. https://doi.org/10.1029/2010JE003778

Kramida, A., Ralchenko, Y., Reader, J., & NIST ASD Team. (2019). *Atomic spectra database version 5.7.1 (NIST, 2019)*. Retrieved from https://physics.nist.gov/asd

Leblanc, F., Chaufray, J. Y., Lilensten, J., Witasse, O., & Bertaux, J. L. (2006). Martian dayglow as seen by the SPICAM UV spectrograph on Mars Express. *Journal of Geophysical Research*, *111*, E09S11. https://doi.org/10.1029/2005JE002664

Leblanc, F., Witasse, O., Lilensten, J., Frahm, R. A., Safaenili, A., Brain, D. A., et al. (2008). Observations of aurorae by SPICAM ultraviolet spectrograph on board Mars Express: Simultaneous ASPERA-3 and MARSIS measurements. *Journal of Geophysical Research*, *113*, A08311. https://doi.org/10.1029/2008JA013033

Lee, R. A., Ajello, J. M., Malone, C. P., Evans, J. S., Veibell, V., Holsclaw, G. M., et al. (2021). Laboratory study of the Cameron bands, the first negative bands, and fourth positive bands in the middle ultraviolet 180–280 nm by electron impact upon CO. *Journal of Geophysical Research: Planets*, *126*, e2020JE006602. https://doi.org/10.1029/2020JE006602

Lilensten, J., Bernard, D., Barthélémy, M., Gronoff, G., Wedlund, C. S., & Opitz, A. (2015). Prediction of blue, red and green aurorae at Mars. *Planetary and Space Science*, *115*, 48–56. https://doi.org/10.1016/j.pss.2015.04.015

Lillis, R. J., & Fang, X. (2015). Electron impact ionization in the Martian atmosphere: Interplay between scattering and crustal magnetic field effects. *Journal of Geophysical Research: Planets*, *120*, 1332–1345. https://doi.org/10.1002/2015JE004841

McClintock, W. E., Schneider, N. M., Holsclaw, G. M., Clarke, J. T., Hoskins, A. C., Stewart, I., et al. (2015). The Imaging Ultraviolet Spectrograph (IUVS) for the MAVEN mission. *Space Science Reviews*, *195*(1–4), 75–124. https://doi.org/10.1007/s11214-014-0098-7

Mitchell, D. L., Mazelle, C., Sauvaud, J.-A., Thocaven, J.-J., Rouzaud, J., Fedorov, A., et al. (2016). The MAVEN solar wind electron analyzer. *Space Science Reviews*, *200*, 495–528. https://doi.org/10.1007/s11214-015-0232-1

Ritter, B., Gérard, J. C., Hubert, B., Rodriguez, L., & Montmessin, F. (2018). Observations of the proton aurora on Mars with SPICAM on board Mars Express. *Geophysical Research Letters*, *45*, 612–619. https://doi.org/10.1002/2017GL076235

Schneider, N., Deighan, J. I., Jain, S. K., Stiepen, A., Stewart, A. I. F., Larson, D., et al. (2015). Discovery of diffuse aurora on Mars. *Science*, *350*, 1–5. https://doi.org/10.1126/science.aad0313

Schneider, N., Jain, S. K., Deighan, J. I., Nasr, C. R., Brain, D. A., Larson, D., et al. (2018). Global aurora on mars during the September 2017 space weather event. *Geophysical Research Letters*, *45*, 7391–7398. https://doi.org/10.1029/2018GL077772

Schneider, N. M., Milby, Z., Jain, S. K., Gérard, J.-C., Soret, L., Brain, D. A., et al. (2021). Discrete aurora on Mars: Insights into their distribution and activity from MAVEN/IUVS observations. *Journal of Geophysical Research: Space Physics*, *126*, e2021JA029428. https://doi.org/10.1029/2021JA029428

Schneider, N., Milby, Z., Jain, S. K., González-Galindo, F., Royer, E., Gérard, J. C., et al. (2020). Imaging of Martian circulation patterns and atmospheric tides through MAVEN/IUVS nightglow observations. *Journal of Geophysical Research: Space Physics*, *125*, e2019JA027318. https://doi.org/10.1029/2019JA027318

Shematovich, V. I., Bisikalo, D. V., & Gérard, J.-C. (1994). A kinetic model of the formation of the hot oxygen geocorona: 1. Quiet geomagnetic conditions. *Journal of Geophysical Research*, *99*(23), 217–228. https://doi.org/10.1029/94JA01769

Shematovich, V. I., Bisikalo, D. V., Gérard, J.-C., Cox, C., Bougher, S. W., & Leblanc, F. (2008). Monte Carlo model of electron transport for the calculation of Mars dayglow emissions. *Journal of Geophysical Research*, *113*, E02011. https://doi.org/10.1029/2007JE002938

Shirai, T., Tabata, T., & Tawara, H. (2001). Analytic cross sections for electron collisions with CO, CO_2, and H_2O relevant to edge plasma impurities. *Atomic Data and Nuclear Data Tables*, *79*(1), 143–184. https://doi.org/10.1006/adnd.2001.0866

Soret, L., Gérard, J.-C., Libert, L., Shematovich, V. I., Bisikalo, D. V., Stiepen, A., & Bertaux, J.-L. (2015). SPICAM observations and modeling of Mars aurorae. *Icarus*, *264*, 398–406. https://doi.org/10.1016/j.icarus.2015.09.023

Stevens, M. H., Evans, J. S., Schneider, N. M., Stewart, A. I. F., Deighan, J., Jain, S. K., et al. (2015). New observations of molecular nitrogen in the Martian upper atmosphere by IUVS on MAVEN. *Geophysical Research Letters*, *42*, 9050–9056. https://doi.org/10.1002/2015GL065319Si

Stiepen, A., Gérard, J.-C., Bougher, S., Montmessin, F., Hubert, B., & Bertaux, J.-L. (2015). Mars thermospheric scale height: CO Cameron and CO_2^+ dayglow observations from Mars Express. *Icarus*, *245*, 295–305. https://doi.org/10.1016/j.icarus.2014.09.051

Stiepen, A., Jain, S. K., Schneider, N. M., Deighan, J. I., González-Galindo, F., Gérard, J.-C., et al. (2017). Nitric oxide nightglow and Martian mesospheric circulation from MAVEN/IUVS observations and LMD-MGCM predictions. *Journal of Geophysical Research: Space Physics*, *122*, 5782–5797. https://doi.org/10.1002/2016JA023523

Weber, T. D. (2020). *The role of crustal magnetic fields in atmospheric Escape from Mars (Doctoral dissertation)*. University of Colorado at Boulder, ProQuest Dissertations & Theses Global. Retrieved from https://scholar.colorado.edu/concern/graduate_thesis_or_dissertations/1544bq39m

Xu, S., Mitchell, D. L., McFadden, J. P., Fillingim, M. O., Andersson, L., Brain, D. A., et al. (2020). Inverted-V electron acceleration events concurring with localized auroral observations at Mars with MAVEN. *Geophysical Research Letters*, *47*, e2020GL087414. https://doi.org/10.1029/2020GL087414